Bioactive Materials 42 (2024) 519–530

Contents lists available at ScienceDirect

Bioactive Materials

journal homepage: www.keaipublishing.com/en/journals/bioactive-materials

Biodegradable WE43 Mg alloy/hydroxyapatite interpenetrating phase composites with reduced hydrogen evolution

Lenka Drotárová [a], Karel Slámečka [a,b], Tomáš Balint [c], Michaela Remešová [a], Radovan Hudák [c], Jozef Živčák [c], Marek Schnitzer [c], Ladislav Čelko [a], Edgar B. Montufar [a,*]

[a] Central European Institute of Technology, Brno University of Technology, Purkyňova 123, Brno, 61200, Czech Republic
[b] Faculty of Mechanical Engineering, Brno University of Technology, Technická 2, Brno 61669, Czech Republic
[c] Department of Biomedical Engineering and Measurement, Faculty of Mechanical Engineering, Technical University of Košice, Letná 9, Košice, 04200, Slovakia

ARTICLE INFO

Keywords:
Magnesium
Biodegradable metal
Calcium phosphate cement
Hydroxyapatite
Composite

ABSTRACT

Biodegradable magnesium implants offer a solution for bone repair without the need for implant removal. However, concerns persist regarding peri-implant gas accumulation, which has limited their widespread clinical acceptance. Consequently, there is a need to minimise the mass of magnesium to reduce the total volume of gas generated around the implants. Incorporating porosity is a direct approach to reducing the mass of the implants, but it also decreases the strength and degradation resistance. This study demonstrates that the infiltration of a calcium phosphate cement into an additively manufactured WE43 Mg alloy scaffold with 75 % porosity, followed by hydrothermal treatment, yields biodegradable magnesium/hydroxyapatite interpenetrating phase composites that generate an order of magnitude less hydrogen gas during degradation than WE43 scaffolds. The enhanced degradation resistance results from magnesium passivation, allowing osteoblast proliferation in indirect contact with composites. Additionally, the composites exhibit a compressive strength 1.8 times greater than that of the scaffolds, falling within the upper range of the compressive strength of cancellous bone. These results emphasise the potential of the new biodegradable interpenetrating phase composites for the fabrication of temporary osteosynthesis devices. Optimizing cement hardening and magnesium passivation during hydrothermal processing is crucial for achieving both high compressive strength and low degradation rate.

1. Introduction

Biodegradable implants serve a temporary structural function in the body and safely degrade upon tissue healing. Unlike non-absorbable implants, biodegradable implants eliminate the need for secondary surgery for their removal, thereby preventing long-term side effects such as sensitivity and infections, reducing healthcare costs, and minimising patient pain and stress. One of the most significant applications of biodegradable implants is in orthopaedics, particularly as temporary osteosynthesis devices. While most biocompatible and biodegradable polymers do not meet the mechanical strength requirements for stable and safe bone fracture reduction, resorbable bioactive ceramics are brittle, rendering both material families unsuitable for load-bearing applications. In contrast, biodegradable metals such as magnesium (Mg) and iron (Fe) based alloys offer the necessary strength and toughness. In addition, Mg alloys have a Young's modulus significantly below Fe alloys and comparable to the Young's modulus of bone, thus minimising the risk of stress shielding that can impede bone fracture healing.

Notably, the WE43 Mg alloy has received CE certification for clinical applications in the fabrication of bioabsorbable osteosynthesis screws [1–3]. WE43 is a high-specific-strength commercial Mg alloy with mechanical properties in the cast state (yield strength of 160 MPa, tensile strength of 250 MPa, Young's modulus of 44 GPa, elongation of 2–6%, and density of 1.8 g/ml) close to those of cortical bone (tensile strength of 150 MPa, Young's modulus of 10–25 GPa, and density of 1.7–2.1 g/ml). Furthermore, the extruded WE43 Mg alloy exhibits a high corrosion fatigue limit in simulated body fluid (40 MPa *vs*. 110 MPa in air) [4]. Mg is combined in this alloy with Y (3.7–4.3 wt%), Nd (2.0–2.5 wt%), and Zr (0.3–1.0 wt%) to improve the mechanical properties and degradation resistance through grain refinement and passivation [5–7]. WE43 Mg alloy implants are biocompatible, promote bone formation,

Peer review under responsibility of KeAi Communications Co., Ltd.
* Corresponding author. CEITEC – BUT, Purkyňova 123, Brno, 61200, Czech Republic.
E-mail address: eb.montufar@ceitec.vutbr.cz (E.B. Montufar).

https://doi.org/10.1016/j.bioactmat.2024.08.048
Received 31 January 2024; Received in revised form 23 August 2024; Accepted 31 August 2024

and undergo uniform degradation at a degradation rate suitable for orthopaedic implants [8–11].

A significant concern when using biodegradable Mg alloys as temporary implants is the peri-implant gas accumulation. Hydrogen is produced due to the cathodic reaction associated with the anodic dissolution of Mg *in vivo*. Excessive initial hydrogen release leads to the formation of gas pockets around the implants. Subsequently, hydrogen is rapidly replaced by carbon dioxide, oxygen, and nitrogen [12,13], which gradually dissipate within two to three weeks of implantation [9,10]. Despite the low degradation rate of the WE43 Mg alloy and the absence of detectable adverse effects from the low concentration of hydrogen *in vivo*, with hydrogen even demonstrating positive antioxidant capacity, transient complications related to gas accumulation limit the widespread clinical acceptance of large biodegradable Mg implants [13]. For example, increased pain levels contribute to patient discomfort, prolong recovery time, and consequently raise the economic burden. Therefore, there is a need to minimise the gas accumulation resulting from Mg degradation. While coatings and surface modifications can regulate the initial abrupt hydrogen release, they only delay or extend the generation of the same volume of gas over a prolonged period [14,15]. In contrast, a significant reduction in the mass of Mg in the implant will directly result in a proportional reduction of the total quantity of degradation products and their negative consequences like peri-implant gas accumulation.

The use of additive manufacturing to create porous Mg implants (scaffolds) provides a direct method for reducing the mass of Mg while producing personalised biodegradable implants. However, porosity introduces important challenges, such as reduced mechanical strength, accelerated degradation rate by increasing the surface area exposed to corrosive electrolyte, and increased risk of implant-related infections. An attractive solution to counteract the drawbacks associated with porosity is filling the 3D network of pores within the Mg scaffolds with a biodegradable reinforcing phase. Among the potential materials, hydroxyapatite is of particular interest as it represents 70 wt% of bone tissue, along with its bioactivity, osteoconductivity, and resorbability [16], and does not form an electrochemical couple with Mg. Biodegradable Mg alloy/hydroxyapatite metal matrix composites have been produced by powder metallurgy [17], casting [18], and squeeze casting [19–22]. However, these composites still contain a high fraction of Mg alloy, ranging from 75 to 92 vol%, due to the challenges of uniformly incorporating a large volume of reinforcing particles without aggregation, thereby producing an equivalent amount of hydrogen as Mg alloy implants.

Recently, significant progress has been made in reducing the Mg fraction and improving control over composite topology through the additive manufacturing of porous hydroxyapatite preforms with ~50 % porosity, which were subsequently infiltrated with Mg and two high-degradation-resistance Mg alloys to create co-continuous Mg/hydroxyapatite interpenetrating phase composites [23]. In contrast to particle-reinforced composites, the constituents in these interpenetrating phase composites form a continuous interdigitated network, enhancing the mechanical reliability of the material. The additively manufactured preforms allowed for precise control of the topology of the composite, thus overcoming the limitations associated with the stochastic addition of discrete particles. Nevertheless, preserving the purity of the constituents was challenging due to the formation of a continuous MgO layer at the Mg/hydroxyapatite interface despite the fast current-assisted metal infiltration method adopted. Furthermore, the need for Mg melting and solidification eliminates the microstructural characteristics that make the extruded Mg alloys strong and corrosion-resistant.

This work introduces the revolutionary infiltration of hydroxyapatite into WE43 Mg alloy scaffolds as an alternative processing route to produce fully biodegradable WE43/hydroxyapatite interpenetrating phase composites with very low content (25 vol% only) of structural biodegradable WE43 Mg alloy. The primary challenge lay in finding a method for hydroxyapatite infiltration different from a powder-metallurgy-based approach, as compaction and sintering will damage and alter the composition and microstructure of the scaffold. To address this issue, a calcium phosphate cement (CPC) is explored herein as a novel solution.

CPCs are injectable and self-hardening materials commonly utilised for bone reconstruction, augmentation of osteosynthesis screws, and vertebroplasty [24]. These materials consist of a solid phase and a liquid phase that, when mixed, form a mouldable and injectable paste, which undergoes a chemical reaction post-implantation, transforming it into a solid monolith. Among the various available CPC formulations (some of them commercial, e.g. Ref. [25]), the cement-based solely on alpha tricalcium phosphate (α-TCP) serves as an excellent model due to its simple formulation [26,27], its transformation into osteoinductive calcium-deficient hydroxyapatite (CDHA) upon setting [28], and wide availability of information on its injectability [29,30]. The mixing of α-TCP powder with poloxamer 407 solutions yields thermoresponsive pastes suitable for bone grafting by minimally invasive surgery [31] and for the extrusion-based additive manufacturing of CDHA scaffolds [32]. In addition to acting as a binder for extrusion, poloxamer 407 reduces the extrusion force when the cement paste is cooled down. Notably, poloxamer 407 is FDA-approved for wound dressing, local drug delivery systems, and embolisation applications [33,34].

The objective of this study is to infiltrate the α-TCP/poloxamer paste into additively manufactured WE43 Mg alloy scaffolds and investigate the effects of three hydrothermal treatments on the *in situ* transformation of α-TCP into CDHA, potential parallel reactions and oxidation of the scaffolds, and phase composition, compressive behaviour, degradation and cytotoxicity of the composites.

The WE43 Mg alloy scaffolds with 75 % porosity were fabricated using laser beam powder bed fusion (LB-PBF) additive manufacturing. While the optimisation of the processing parameters remains an ongoing research topic, this study focuses on a specific set of parameters selected based on our previous unpublished work. The microstructural, mechanical, degradation, and *in vitro* characterisations of the as-printed and hydrothermally treated scaffolds are presented alongside the characterisation of the composites for comparison, shedding light on the currently poorly understood behaviour of the additively manufactured WE43 Mg alloy and its use in WE43/hydroxyapatite composites.

2. Materials and methods

2.1. Biodegradable Mg alloy scaffolds

The fabrication of the biodegradable scaffolds utilised spherical WE43 Mg alloy powder (HANA AMT Co., Ltd., South Korea) with a particle size ranging from 27 to 59 μm in the as-received state. According to the supplier, the content of alloying elements in the powder was 4.2 wt% Y, 2.4 wt% Nd, 1.4 wt% Gd, and 0.4 wt% Zr, while the total content of harmful impurities (Fe, Cu, and Ni) was determined to be 0.013 wt% using spark discharge optical emission spectroscopy. A Voronoi lattice design was adopted to create the virtual model of the scaffolds (cylinders with an outline diameter of 7.5 mm and a length of 70 mm) [35]. The thickness of struts was set to 250 μm, with 800 seeding points, resulting in a design porosity of 75 %. The scaffolds were fabricated by LB-PBF additive manufacturing using an Aconity TWO device (Aconity 3D, Germany) equipped with a 250 W ytterbium fibre laser (IPG Laser GmbH, Germany) operating in the continuous wave mode. The laser, with a Gaussian profile and a wavelength of 1070 nm, had a spot size diameter of 130 μm focused on the processing plane. Argon 4.6 (99.996 %) was used as a protective gas during the fabrication process to prevent oxidation, with an argon flow rate of 50 l/min. The overpressure in the building chamber was 0.6 MPa, and the residual oxygen content was maintained below 500 ppm. The scaffolds were produced on a preheated WE43 platform at 520 °C, using a laser power of 100 W, a scanning speed of 500 mm/s, a hatch spacing of 40 μm, a hatch offset of

60 μm, and a layer thickness of 30 μm. Subsequently, the scaffolds were removed from the platform by wire-cutting and cut with a SiC disc into cylinders with a height of 12 mm.

2.2. Self-hardening injectable paste and optimisation of infiltration

The pastes used for infiltrating the scaffolds consisted of α-TCP powder mixed with a poloxamer 407 solution (40 wt%, Sigma Aldrich, USA). The α-TCP powder was synthesised by a solid-state reaction at 1400 °C for 2 h between $CaCO_3$ and $CaHPO_4$, followed by air quenching. The produced α-TCP block was dry milled (Fritsch Pulverisette 6, Germany) at 450 rpm for 15 min, and then the powder fraction below 32 μm was separated by sieving. Subsequently, the pastes were prepared at different liquid-to-powder (L/P) ratios (0.35–0.60 ml/g) to determine the lowest ratio required for complete infiltration of the paste into the Mg alloy scaffold by injection.

During the infiltration process, the α-TCP/poloxamer paste (2 ml) was introduced into a standard syringe without a nozzle, cooled to 4 °C, and injected into the scaffold. The lateral surface of the scaffold was sealed to prevent radial paste extrusion, ensuring that the paste flowed along the long axis from one end to the other. The infiltrated scaffolds were hydrothermally treated to obtain WE43/CDHA composites by the *in situ* chemical transformation of α-TCP into CDHA (Eq. (1)). Three hydrothermal treatments were studied: 1) immersion in distilled water at 37 °C for 7 days (Mg/CDHA-37), 2) immersion in distilled water at 90 °C for 6 h (Mg/CDHA-90), and 3) exposure to a moist atmosphere inside an autoclave at 190 °C for 30 min (Mg/CDHA-190). These combinations were selected based on the available information on the conversion rate of α-TCP at different temperatures [32,36], with the aim of minimising the corrosion time of Mg. In addition, non-infiltrated (empty) scaffolds and α-TCP/poloxamer pastes shaped into cylinders inside moulds (prepared at the same L/P ratio as the infiltrated pastes) were hydrothermally treated alongside the infiltrated scaffolds as controls. Afterwards, all the materials were rinsed with distilled water and dried at 37 °C for 24 h.

$$3\alpha\text{-}Ca_3(PO_4)_2 + H_2O \rightarrow Ca_9(HPO_4)(PO_4)_5(OH) \quad (1)$$

2.3. Microstructural characterisation

The cross-sections of the scaffolds were prepared by means of the cold mounting technique followed by metallographic methods, including final polishing with colloidal silica suspension (0.25 μm particle size) and etching with an acetic picral solution. The microstructure and surface morphology of the samples were examined with two opto-digital light microscopes (LM; DSX510 and DSX110, Olympus, Japan) in bright-field (BF) mode and a scanning electron microscope (SEM; Mira3, Tescan, Czech Republic) in secondary electron (SE) and back-scattered electron (BSE) modes with an accelerating voltage of 10 kV. The samples were coated with a nanometric carbon layer prior to the SEM observation to prevent charging. Chemical elemental analysis was conducted using spark discharge optical emission spectroscopy (Q4 TASMAN, Bruker, USA) on flat samples mechanically compacted at a pressure of 10 MPa applied for 1 min. The crystalline phases were identified by X-ray diffraction (XRD; SmartLab 3 kW, Rigaku, Japan). Measurements were carried out in the Bragg-Brentano parafocusing geometry at 40 kV and 30 mA, producing CuKα radiation with $\lambda = 0.154$ nm. The scanning 2θ range was set between 10 and 90°, with a step of 0.02° and a scanning speed of 4°/min. Phase identification was performed in the HighScore Plus software (Panalytical, Netherlands) using the ICSD database.

The porosity of the scaffolds was measured ($n = 5$) by gravimetric analysis according to Eq. (2).

$$P = (1 - D_{apparent}/D_{skeletal}) * 100 \quad (2)$$

where $D_{apparent}$ is the apparent density of the scaffold, calculated by dividing the mass by the bulk volume, and $D_{skeletal}$ is the theoretical density of the WE43 Mg alloy. The height and diameter of the scaffolds were measured with a calliper to determine the bulk volume.

2.4. Mechanical characterisation

The composites, the control Mg alloy scaffolds, and the control CDHA monoliths were tested in compression ($n = 5$). The tests were conducted in dry state at room temperature using a servohydraulic testing system (Instron 8874, USA) at a crosshead speed of 1 mm/min. The compressive strength was derived from the obtained stress-strain curves as the first stress peak maximum. Images of the samples during the compression test were captured with a digital camera, and compressed samples were observed using SEM.

2.5. Degradation characterisation

The degradation rate of the Mg alloy scaffolds (both as-printed and hydrothermally treated at 190 °C) and Mg/CDHA-190 composites was determined using a hydrogen evolution test at 37 °C ($n = 3$). Each cylindrical sample (diameter of 7.3 mm and height of 12 mm) was individually immersed in 500 ml of Hank's simulated body fluid (HSBF). The solution was produced in-house using analytical grade reagents from Lach-Ner (Czech Republic) with the following composition: 8.00 g/l NaCl, 0.40 g/l KCl, 0.35 g/l $NaHCO_3$, 0.06 g/l KH_2PO_4, 0.06 g/l $Na_2HPO_4{\cdot}2H_2O$, 0.14 g/l $CaCl_2$, 0.10 g/l $MgCl_2{\cdot}6H_2O$ and 0.06 g/l $MgSO_4{\cdot}7H_2O$. The pH of the HSBF and the volume of hydrogen gas produced by the galvanic dissolution of Mg were recorded for 15 days. The degradation rate, expressed in mm/year, was calculated using the following equation [37]:

$$Degradation\ rate = 2.279\ V_H \quad (3)$$

where V_H is the volume of hydrogen (ml) generated per unit of sample surface area (cm^2) exposed to the electrolyte per unit of time (days). The exposed surface area of the scaffolds was determined from the virtual model of the scaffold used for fabrication (effective surface area of 9.6 cm^2). For the composite, the geometric surface area of the cylindrical sample was used for the calculations (3.6 cm^2).

Following the degradation test, the samples were rinsed with distilled water, placed on adsorbent tissue to remove excess water, documented with an opto-digital LM, and dried at 37 °C for 3 days. The compression test of the materials after 3 days of degradation in HSBF was performed following the procedure outlined in section 2.4.

2.6. Cytocompatibility test

Human fetal osteoblast cell line hFOB 1.19 (ATCC, Manassas, USA) in cell passage 5 was used to determine cell proliferation in indirect contact with Mg alloy scaffolds (both as-printed and hydrothermally treated at 190 °C) and Mg/CDHA-190 composites. The cell culture medium consisted of Dulbecco's Modified Eagle Medium/Ham's nutrient mixture F-12 without phenol red (DMEM/F12, 1:1, ThermoFisher, USA), supplemented with 10 % fetal bovine serum (FBS, Sigma Aldrich, USA) and 0.1 % gentamicin (Sigma Aldrich, USA). The cells were seeded at a density of 5×10^4 cells/well in a 48-well microplate (ThermoFisher, USA) and cultivated at 37 °C in a humified atmosphere of 5 % CO_2 for 24 h to allow cell attachment. Afterwards, the cells were rinsed three times with phosphate buffer saline (PBS) and 1 ml of fresh medium was added to each well. A single material sample (diameter of 7.3 mm, height of 3 mm, disinfected by immersion in 70 % ethanol for 30 min) was individually added to each well containing the cells. Cell metabolic activity was determined by the resazurin assay after 1, 3, and 7 days of cultivation ($n = 3$) with medium renewal every 2 days. At each time point, the material was removed with tweezers, the cells were

rinsed three times with PBS, and 500 μl of 10 % resazurin solution (Sigma Aldrich, USA) in DMEM/F12 medium was added to each well. The plates were incubated for 4 h at 37 °C in 5 % CO_2, protected from light. After incubation, 150 μl of each incubated resazurin solution was transferred into a well of a 96-well microplate, and the fluorescence of the solution was measured with a microplate reader (BioTek Synergy H1, USA; excitation at 560 nm and emission at 590 nm). The results were expressed as relative fold changes compared to the cell metabolic activity obtained on tissue culture polystyrene (TCPS, without materials) at 1 day. Materials immersed in medium without cells served as references.

3. Results

3.1. Microstructure of WE43 Mg alloy scaffolds

The as-printed Mg alloy scaffolds (Fig. 1a) had an average outer diameter of 7.25 ± 0.02 mm and an average porosity of 75.3 ± 0.4 %, closely aligning with the digital design. The struts were nearly fully dense, showing minimal small intra-strut pores and no apparent cracks (Fig. 1b and c). The scanning tracks and melt pool boundaries were evident in the cross-section of the struts (Fig. 1c). The microstructure was heterogeneous with multiple fusion interfaces (Fig. 1c). The melt pools exhibited a dendritic sub-microstructure with a varying dendrite orientation between adjacent pools (Fig. 1d). Numerous mechanically stable powder adhesions were observed on the surface of the struts (Fig. 1b). The elemental analysis of the as-printed scaffolds showed a slight increase in the content of alloying elements and impurities compared to the feedstock powder (Table 1), related to Mg evaporation during LB-PBF. In particular, the Fe content exceeded the tolerance limit for the corrosion resistance of as-cast Mg (0.018 wt%).

3.2. α-TCP/poloxamer paste infiltration

Infiltration of the α-TCP pastes prepared with a L/P ratio below 0.50 ml/g was found to be unattainable. In general, the pastes exhibited limited flow, extending less than half of the length of the scaffolds, as the force needed to inject the paste exceeded the strength of the syringe piston at this point. Complete infiltration of the scaffolds was successfully achieved at a L/P ratio of 0.50 ml/g (Fig. 2a). In this case, the α-TCP paste flowed steadily, adapting to the pore geometry (Fig. 2b–c) and the rough surface of the struts (Fig. 2d). The presence of a convex meniscus at certain interfaces (Fig. 2c) suggested a repulsive contact between the α-TCP paste and the Mg alloy. Nevertheless, the paste established a continuous contact with the struts, facilitated by the roughness provided by the powder adhesions (Fig. 2d).

The evolution of hydrogen gas caused the α-TCP paste to be expelled from the scaffolds during hydrothermal treatment in water at 37 °C (Fig. 2e). Therefore, these composites were not subjected to mechanical and degradation characterisations. In contrast, the α-TCP paste hardened within the scaffolds when they were immersed in water at 90 °C or placed in an autoclave at 190 °C (Fig. 2f), resulting in the formation of Mg/hydroxyapatite interpenetrating phase composites. The cross-section of the Mg/CDHA-190 composite confirmed that the inter-strut space of the Mg alloy scaffold was completely filled with hydroxyapatite (Fig. 2g).

Table 1
Elemental chemical composition of the feedstock powder and as-printed Mg alloy scaffolds.

Material	Element (wt%)				
	Mg	Y	Nd	Zr	Fe
Powder	balance	3.121	1.320	0.506	0.013
As-printed scaffold	balance	5.167	1.730	0.651	0.023

3.3. Microstructure of hydrothermally treated materials

The Mg alloy scaffolds corroded during the hydrothermal treatments, producing a corrosion layer on the struts (Fig. 3). In addition, a significant amount of white corrosion product was observed on the surface of the struts (Fig. 3a–b). The corrosion layer was continuous, dense, adherent, and had an average thickness of 33 ± 3 μm (Fig. 3c–d). While the layer displayed several vertical cracks, few horizontal cracks were visible. The microstructure of the hydrothermally treated struts (Fig. 3d) was the same as that observed in the as-printed scaffolds (Fig. 1d).

The corrosion layer was also evident in the composites at the Mg/CDHA interface and on the struts observed on the composite surface (Fig. 4). Notably, no interfacial cracks were seen, and a smooth microstructural transition from the corrosion layer to the CDHA was noted (Fig. 4d–f). Nonetheless, contact discontinuities in the form of oval pores, which were linked to hydrogen release during the hydrothermal treatments, were observed at the interfaces (red arrows in Fig. 4a–c).

At the microstructural scale, the ceramic component in the Mg/CDHA-190 composite developed an entangled network of needle-like hydroxyapatite crystals characteristic of the α-TCP transformation into CDHA (Fig. 5d). In contrast, the ceramic component in the Mg/CDHA-90 composite preserved the morphology of compacted polyhedral α-TCP particles (Fig. 5c). XRD analysis confirmed the limited transformation of α-TCP into CDHA in this case, whereas the control monoliths (CDHA-90) exhibited a significantly advanced transformation, although it was still incomplete, as the main diffraction peak of α-TCP was clearly identified in the diffractogram (Fig. 5a). Clear hydroxyapatite diffraction peaks were observed in the XRD pattern of the Mg/CDHA-190 composite, along with peaks related to α-TCP and β-TCP (Fig. 5b). The α-TCP peaks arose due to an incomplete chemical transformation into CDHA, while the β-TCP peaks indicated the partial α-TCP to β-TCP polymorph phase transformation in the autoclave. The lower degree of conversion of α-TCP in the composites was also evident when comparing the crystalline composition of Mg/CDHA-190 with the CDHA-190 control, which only exhibited the characteristic diffraction peaks of hydroxyapatite and β-TCP, without the presence of α-TCP, despite the hydrothermal treatment lasting only 30 min.

XRD analysis enabled the identification of the corrosion products generated on the Mg surfaces (both in the empty scaffolds and the composites) as a mixture of magnesium hydroxide ($Mg(OH)_2$), magnesium carbonate ($MgCO_3$), and a minor amount of magnesium oxide (MgO). These products showed increased diffraction intensities with the

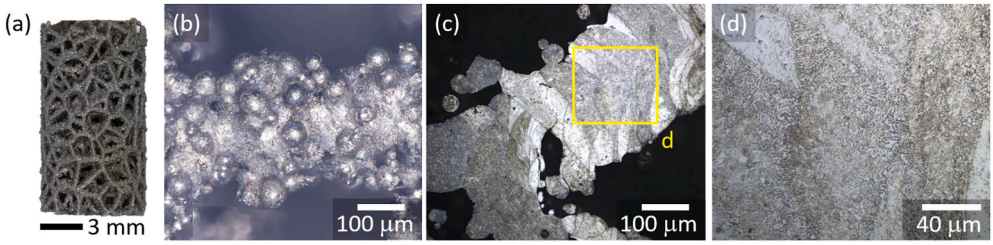

Fig. 1. LM images of (a) as-printed WE43 Mg alloy scaffold, (b) detail of the surface morphology of the struts, (c–d) microstructure of the strut cross-section.

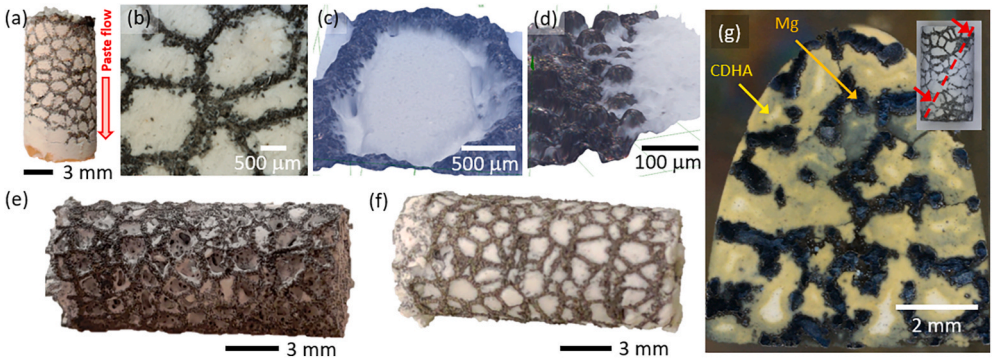

Fig. 2. (a) Mg alloy scaffold infiltrated with α-TCP paste (L/P = 0.50 ml/g), (b–d) detail of the conformation of the α-TCP paste to the porosity and surface of the scaffolds, (e) composite after 24 h of immersion in water at 37 °C, (f) surface and (g) cross-section at 45° of the composite after 30 min of incubation in an autoclave at 190 °C. (a, e, f) digital camera, (b–d, g) LM, and (c, d) 3D view.

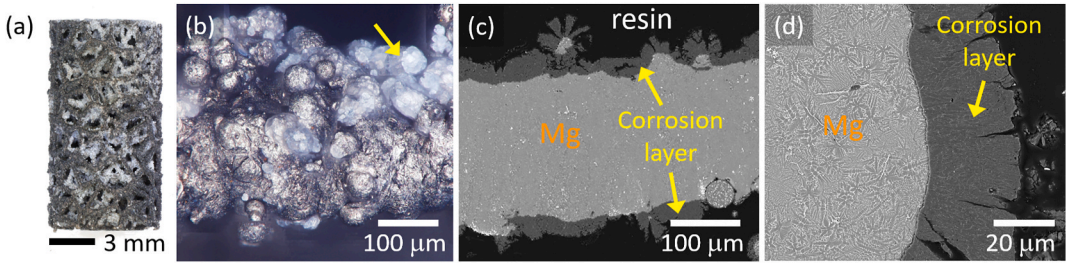

Fig. 3. (a) WE43 Mg alloy scaffold after incubation in an autoclave at 190 °C for 30 min (LM), (b) detail of the surface morphology of the struts (LM), and (c, d) detail of the microstructure of the strut cross-section (SEM - BSE). Yellow arrows point to the corrosion products and the corrosion layer.

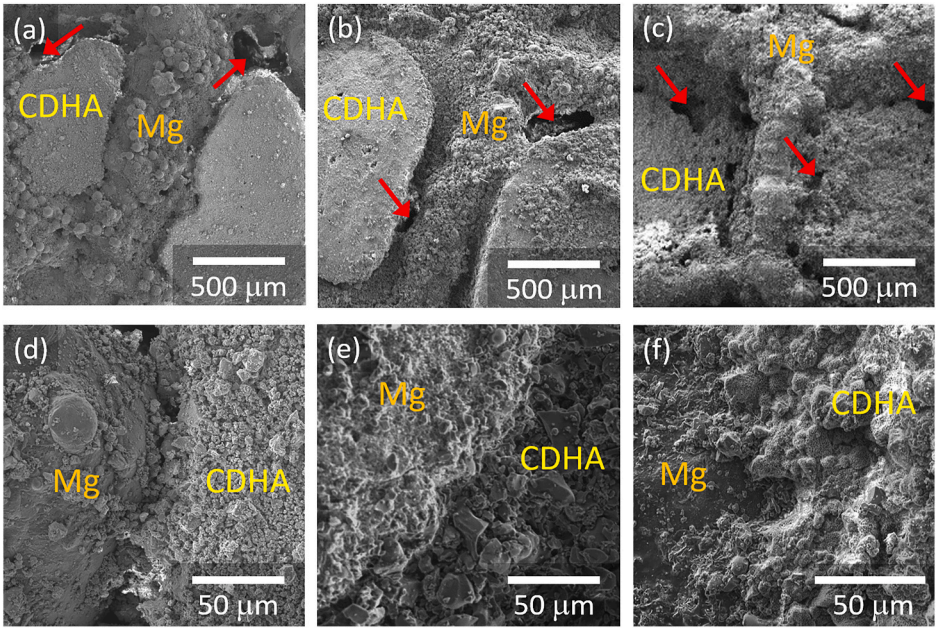

Fig. 4. SEM - SE images of the Mg/CDHA composites after hydrothermal treatment at (a, d) 37 °C for 7 days (Mg/CDHA-37), (b, e) 90 °C for 6 h (Mg/CDHA-90), and (c, f) 190 °C for 30 min (Mg/CDHA-190). Red arrows point to the pores at the Mg/CDHA interface produced by hydrogen release before α-TCP hardening.

increment of the hydrothermal treatment temperature (Fig. 5a–b).

3.4. Mechanical evaluation

The as-printed Mg alloy scaffolds (Mg-as-printed) and the control scaffolds immersed in water at 90 °C for 6 h (Mg-90) exhibited similar stress-strain responses (Fig. 6a). These scaffolds displayed a distinct yield stress, a maximum stress peak, followed by a stress decrease and a serrated plateau, extending up to at least 30 % strain at nearly constant flow stress, without developing a densification region. Interestingly, the hydrothermal treatments slightly increased the compressive strength of the Mg alloy scaffolds (Fig. 6d). Despite the modest improvement, the scaffolds treated in the autoclave at 190 °C for 30 min (Mg-190) displayed sudden failure soon after reaching the peak stress (Fig. 6a).

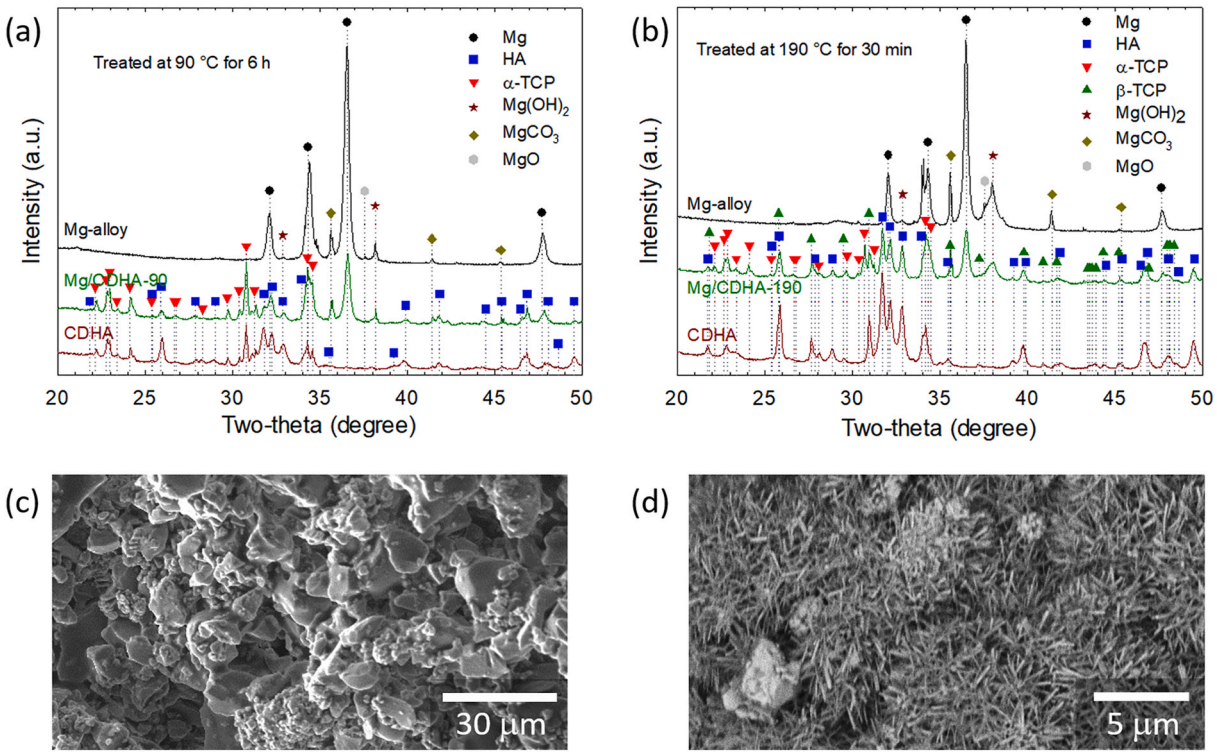

Fig. 5. (a–b) XRD patterns of the Mg alloy scaffolds, Mg/CDHA composites and control CDHA monoliths hydrothermally treated at (a) 90 °C for 6 h and (b) 190 °C for 30 min, (c–d) SEM - SE images of the ceramic phase in the composites (c) Mg/CDHA-90 and (d) Mg/CDHA-190.

The CDHA monoliths exhibited brittle failure (Fig. 6b), with a significant difference in compressive strength depending on the hydrothermal treatment condition (Fig. 6b and d). The CDHA-190 monoliths were nearly 2.5 times stronger than the CDHA-90 monoliths, confirming the effectiveness of the autoclave in transforming α-TCP into CDHA.

The Mg/CDHA composites were stronger than all the control materials except the CDHA-190 monoliths (Fig. 6d). Unlike the bare CDHA, and similarly to the as-printed Mg alloy scaffolds, the composites underwent 30 % strain at high flow stresses (Fig. 6c). Furthermore, the flow stress in the composites tended to increase at the plateau instead of the more serrated response observed in the as-printed and hydrothermally treated (Mg-90) Mg alloy scaffolds. The Mg/CDHA-190 composites were stronger than the Mg/CDHA-90 counterparts (Fig. 6d). These results suggest that CDHA significantly enhances the load-bearing capacity of the composite, while even a brittle continuous Mg component still provides high damage tolerance.

The failure of the as-printed Mg alloy scaffolds was bending dominant (Fig. 7a), with strut buckling and the formation of inclined macroscopic shear planes (insets in Fig. 6a). Cracks were located near the fusion interfaces (Fig. 7a–b), and the fracture surfaces exhibited limited plastic deformation before failure (Fig. 7c). The fracture surface of the Mg/CDHA-190 composites was complex (Fig. 7d). Macroscopically, the composite showed a uniaxial compression failure (insets in Fig. 6c) and its fracture surface was very rough, revealing numerous fractured struts within the composite (brighter regions in Fig. 7d). Moreover, the struts were encased in a compact corrosion layer, which was interlocked with the CDHA phase (Fig. 7e). At the composite periphery, CDHA was often detached from the fractured struts at large strains (Fig. 7f and insets in Fig. 6c).

3.5. *In vitro degradation*

The hydrogen evolution was one order of magnitude less severe in the Mg-190 scaffold (hydrothermally treated in an autoclave) than in the as-printed Mg scaffold (Fig. 8a). Additionally, the hydrogen evolution was further reduced by 50 % in the case of the Mg/CDHA-190 composites (with respect to the Mg-190 scaffold) owing to the incorporation of CDHA. The degradation rate of the as-printed Mg alloy scaffolds abruptly increased during the first hour of immersion, peaking at 83.3 ± 6.6 mm/year, before gradually decreasing to 17.8 ± 1.2 mm/year by day 15 (Fig. 8b). In contrast, the degradation rate of the Mg-190 scaffolds showed a less severe initial increase, requiring about 4.5 h to reach a maximum of 8.6 ± 1.8 mm/year. Afterwards, the degradation rate slowly decreased to a value of 4.2 ± 1.7 mm/year by day 15. The degradation rate of the composites reached a maximum of 13.3 ± 4.1 mm/year after about 2 h of immersion, dropped below 5 mm/year after 24 h, and stabilised at 1.9 ± 1.0 mm/year. Reflecting the degradation rates, the Mg/CDHA-190 composite generated the smallest and slowest pH increase of the HSBF, followed by the Mg-190 scaffold. In contrast, the Mg-as-printed scaffold showed the largest and fastest increase in pH (Fig. 8c).

While the appearance of the as-printed and autoclave-treated scaffolds changed significantly due to the severe degradation of the Mg struts (Fig. 8d and e, respectively), the appearance of the composites remained almost unchanged after 15 days of degradation (Fig. 8f), with only occasional CDHA local detachments observed. The degradation products filled the inter-strut space of the scaffolds (Fig. 8d and e), while in the composite, their formation was limited to the surface of the external struts (Fig. 8f). Degradation had a negative impact on the mechanical properties of the materials (Fig. 9), resulting in a 26 %, 3 %, and 31 % reduction in the compressive strength of the Mg-as-printed scaffolds, Mg-190 scaffolds (hydrothermally treated in an autoclave), and Mg/CDHA-190 composites, respectively, after 3 days of degradation. Notably, the degradation-induced weakening effect was less pronounced in the Mg-190 scaffolds, which also exhibited prolonged deformation after degradation instead of sudden failure (Fig. 9b). Conversely, the stress in the Mg/CDHA-190 composites after degradation decreased more rapidly beyond the peak stress, before gradually increasing to form the plateau (Fig. 9c).

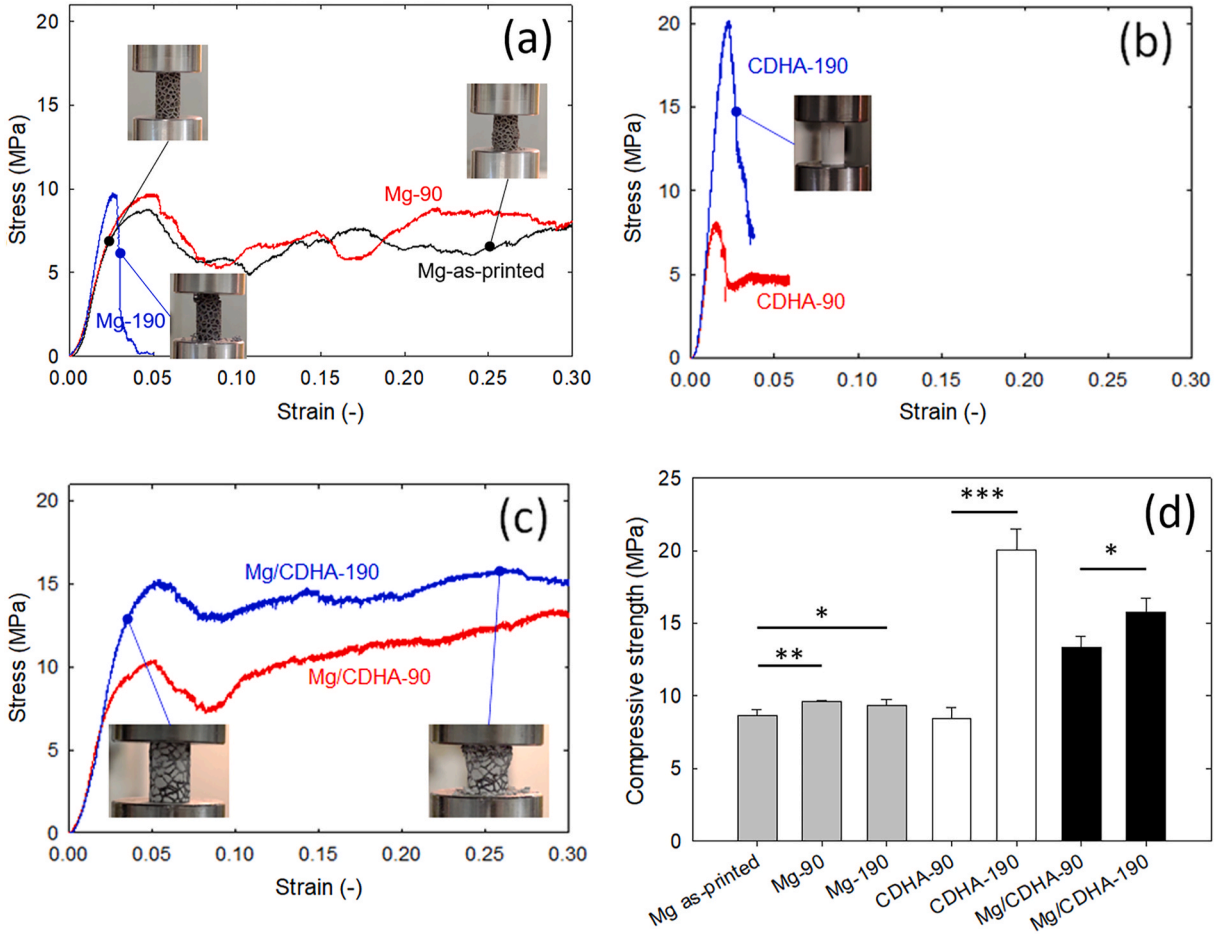

Fig. 6. (a–c) Stress-strain curves of the materials after different processing conditions (a) Mg alloy scaffolds, (b) CDHA monoliths, and (c) Mg/CDHA composites. The insets show the samples at different deformations (digital camera). (d) Compressive strength (first peak stress; average ± SD ($n = 5$); Student t-test: $*p < 0.05$, $**p < 0.01$, $***p < 0.001$).

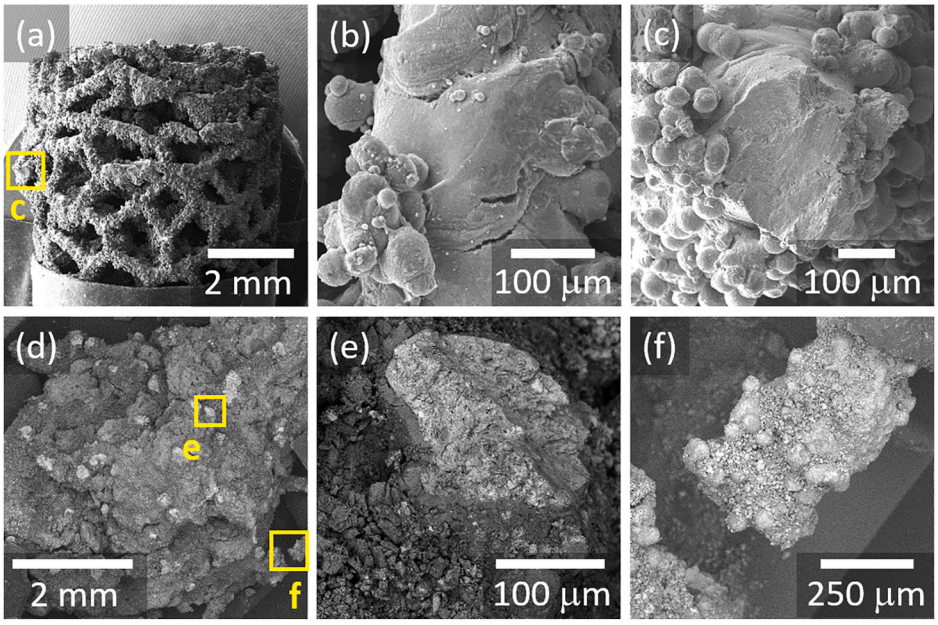

Fig. 7. (a–c) As-printed Mg alloy scaffold (SEM - SE), and (d–f) Mg/CDHA-190 composite (SEM - BSE) after compression test. The squares in (a) and (d) indicate the areas observed at higher magnifications.

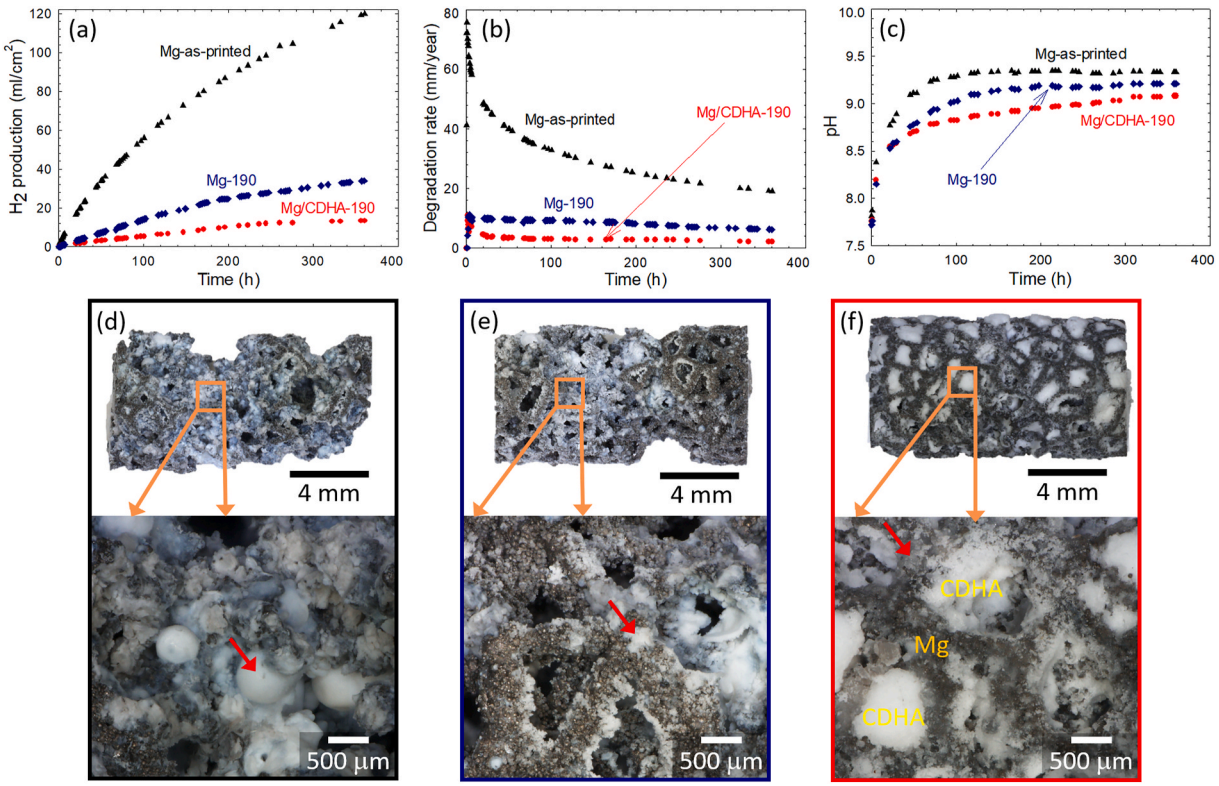

Fig. 8. (a) Hydrogen evolution during degradation, (b) degradation rate calculated from the hydrogen evolution, and (c) pH of the HSBF during the degradation test. LM images after 15 days of degradation of (d) Mg-as-printed scaffold, (e) Mg-190 scaffold (hydrothermally treated in the autoclave), and (f) Mg/CDHA-190 composite. Red arrows point to the corrosion products.

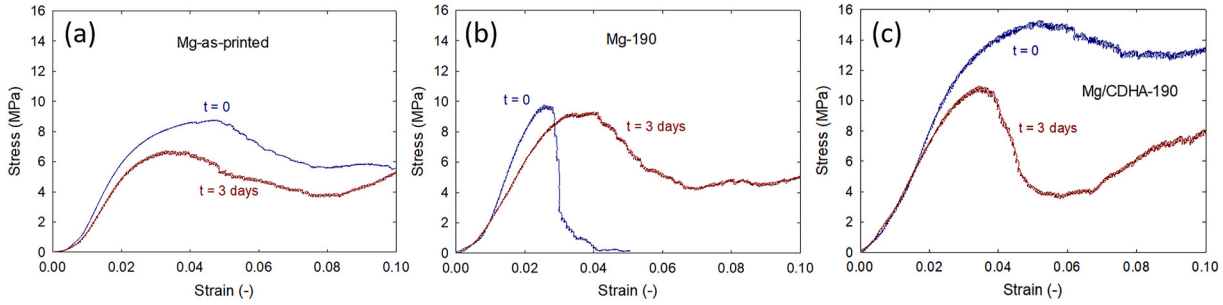

Fig. 9. Stress-strain curves before and after 3 days of degradation in HSBF (a) Mg-as-printed scaffolds, (b) Mg-190 scaffolds (hydrothermally treated in the autoclave), and (c) Mg/CDHA-190 composites.

3.6. Cytocompatibility test

The cell metabolic activity in indirect contact with the Mg-as-printed scaffolds was lower than in the TCPS and decreased over time (Fig. 10). In contrast, the cell metabolic activity in indirect contact with the Mg-190 scaffolds was similar to that of the TCPS and increased over time (Fig. 10). However, it did not reach the same level as the TCPS by day 7. The cell metabolic activity in indirect contact with the Mg/CDHA-190 composites was lower than that of the TCPS and other materials on days 1 and 3, but increased by day 7, reaching a similar average value to that of the TCPS (Fig. 10). Overall, both Mg-190 scaffolds and Mg/CDHA-190 composites were cytocompatible, enabling the proliferation of osteoblasts, while the as-printed Mg scaffolds were cytotoxic.

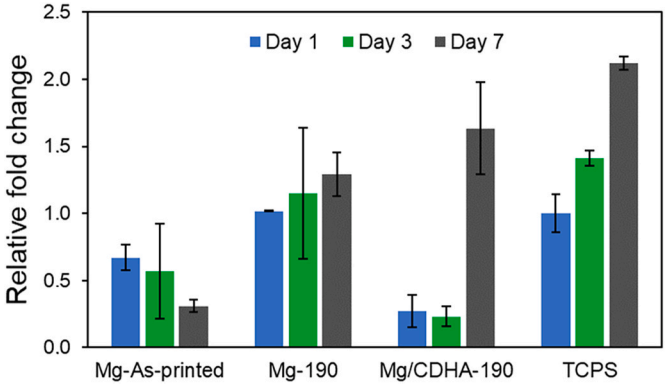

Fig. 10. Osteoblasts proliferation in indirect contact with the Mg alloy scaffolds and the Mg/CDHA-190 composite. The results are expressed as relative fold changes compared to the cell metabolic activity obtained on TCPS on day 1.

4. Discussion

WE43 Mg alloy and hydroxyapatite are two important materials for bone repair, used to fabricate biodegradable implants suitable for

temporal orthopaedic applications. Filling the pores within Mg alloy scaffolds with an α-TCP paste is an attractive route to produce fully biodegradable WE43/CDHA interpenetrating phase composites that generate a minimal amount of hydrogen and exhibit a higher compressive strength and better degradation resistance compared to empty Mg alloy scaffolds. This study demonstrates that the WE43/CDHA interpenetrating phase composites offer several advantages over the individual material components.

The WE43 Mg alloy scaffolds with a Voronoi design were produced with high dimensional accuracy and reproducibility using the LB-PBF method. The Voronoi scaffold exhibits a trabecular-like structure akin to cancellous bone (Fig. 1a), which is advantageous for osteogenesis [38]. The as-printed scaffolds displayed bending-dominant mechanical behaviour in agreement with findings from experimental and numerical studies on metallic Voronoi structures with similar design porosity produced by the LB-PBF method [39–41]. Cracks were localised at or near the fusion interfaces, indicating them as the weakest microstructural feature. The compressive strength of the scaffolds resembled that of comparable WE43 Mg alloy scaffolds with a diamond unit cell and equivalent porosity recently produced by LB-PBF [42]. A slight increase in compressive strength after short-term hydrothermal treatment at 90 and 190 °C was likely due to the corrosion layer filling surface imperfections that could otherwise act as stress concentrators.

The Mg alloy scaffolds with 75 % porosity were significantly weaker (compressive strength of 8.6 *vs.* approximately 160 MPa [9]) and less degradation resistant (degradation rate of 17.8 *vs.* 0.25–2.2 mm/year [43,44]) than cast and extruded WE43 Mg alloy dense monoliths due to the reduced effective cross-sectional area for load-bearing, heterogeneous microstructure, and increased surface area for electrochemical reactions. Therefore, despite lower hydrogen evolution volume due to the much lower mass of Mg compared to dense implants, the Mg alloy scaffolds currently lack sufficient strength and degradation resistance for clinical applications. Strategies for increasing the strength without adding Mg material include promoting bonding between layers to prevent cracking at the fusion interfaces and increasing the regularity of Voronoi cells, which has the potential to create stronger structures [39,45]. Nonetheless, the most effective approach is to redesign the scaffold, as there are structures stronger than the Voronoi design, including those based on triply periodic minimal surfaces [41,46] or novel hybrid structural designs, e.g. Ref. [40].

The as-printed scaffolds showed severe degradation after 15 days of immersion in HSBF with an evident loss of structural integrity (Fig. 8d). Despite the fast degradation, these scaffolds still exhibited better corrosion resistance than previously reported scaffolds with a diamond unit cell and equivalent porosity, which disintegrated into small pieces after 16 h in HSBF [42]. Moreover, the scaffolds in this study maintained a load-bearing capacity after 3 days of degradation (Fig. 9). Given the similar porosity, the difference in degradation resistance may be attributed to microstructural and architectural differences. Here, the main factors contributing to the low degradation resistance of the WE43 scaffolds include the heterogeneous microstructure with multiple fusion interfaces, varying dendrite orientation between neighbouring melting pools, and relatively high Fe content that together trigger microgalvanic reactions, as well as powder adhesions that increase the effective surface area for these reactions. In addition, the corrosion resistance of WE43 objects (dense monoliths and scaffolds) produced by LB-PBF is lower than that of cast and extruded equivalents due to the precipitation of compounds of Mg with Nd, Gd, and Y (both at the grain boundaries and within the grains), and Y and Y-Zr oxides [42,47–50]. Therefore, optimisation of the LB-PBF process and development of post-printing heat treatments that improve the microstructural homogeneity and reduce the surface roughness are needed to improve the degradation resistance.

The short hydrothermal treatment in the autoclave generates a dense corrosion layer on the scaffold struts that reduces the degradation rate by an order of magnitude. The corrosion layer also improves the mechanical performance due to reduced stress concentration, and the hydrothermally treated scaffolds retained nearly 100 % of their compressive strength and exhibited reduced brittleness after 3 days of degradation (Fig. 9b). However, after 15 days of immersion, they showed a similar structural loss as the as-printed scaffolds. There is evidence that the compactness, thickness, and adherence of coatings formed by hydrothermal treatment efficiently protect Mg alloys against degradation especially during the first 24 h of immersion [51,52]. In this context, the corrosion layer formed on the scaffolds herein had an equivalent composition, thickness, and adherence, thereby improving corrosion resistance.

The Mg/CDHA-190 composite has a degradation resistance similar to the dense WE43 Mg alloy in the cast and extruded state (degradation rate of 1.9 *vs.* 0.25–2.2 mm/year [43,44]) and a compressive strength higher than that of the as-printed scaffolds (Fig. 6d). Previous studies have demonstrated that the degradation resistance of Mg-matrix composites reinforced with hydroxyapatite particles improves because of the formation of a compact and stable $Mg(OH)_2$ corrosion layer enriched with apatite [53]. Apatite deposition during degradation is triggered by the bioactivity of hydroxyapatite in contact with physiological fluids. The composite layer offers more efficient protection to the Mg surface from the corrosive environment than $Mg(OH)_2$ alone and fills the corrosion pits and valleys [53]. Therefore, the hydrothermal treatment designed to transform α-TCP into CDHA generates, like in the case of the as-printed scaffold, a continuous interfacial layer that efficiently passivates Mg, thereby enhancing the corrosion resistance of the composites. The stability of the passivation layer provided by the interpenetration of phases plays a key role in enhancing the degradation resistance, preventing localised corrosion and loss of structural integrity. Another contributing factor providing additional corrosion resistance to the composite is the reduction in the Mg surface area exposed to the electrolyte. However, the impact of this mechanism is expected to be limited as CDHA is intrinsically porous [32,36], allowing electrolyte permeation towards the Mg surfaces within the composite. While further optimisation is necessary to reduce the composite degradation to clinically acceptable levels (hydrogen evolution volume below 0.01 $ml/cm^2/day$ [54]), the improvement with respect to LB-PBF WE43 scaffolds is significant (a hydrogen evolution of approximately 20 $ml/cm^2/day$ *vs.* 2 $ml/cm^2/day$ during the first 24 h of immersion).

The lower degradation of the hydrothermally treated scaffold and composite was associated with a lower alkalisation of the electrolyte. However, the alkalisation of the HSBF was significantly higher than that generated by LB-PBF WE43 dense objects immersed in conventional simulated body fluid [55]. Conversely, the alkalisation generated by the as-printed scaffold was lower than that produced by equivalent WE43 scaffolds with diamond unit cell [42]. The lower alkalinisation from the hydrothermally treated scaffold allowed osteoblasts to achieve a cell metabolic activity equivalent to that observed in the control (TCPS), thus reflecting a full cytocompatibility of the material. The cytocompatibility of the hydrothermally treated scaffold was even superior to the cytocompatibility of the LB-PBF WE43 dense alloy after 1 day of culture (approximately 75 % of the control [55]). Furthermore, the metabolic activity of the osteoblasts in indirect contact with the treated scaffold increased over time, indicating their proliferation. However, by day 7, the cell metabolic activity was 61 % of the control, falling below the cytocompatibility threshold of 70 % as per ISO standard 10993-5. In contrast, the osteoblast metabolic activity after 1 day of contact with the as-printed scaffold was 67 % of the control and decreased over time as a signal of material cytotoxicity, likely due to abrupt Mg leaching causing an increase in the osmolality and alkalinisation of the cell culture medium above normal values for mammalian cells cultivation (osmolality between 260 and 320 mOsm [56] and pH between 7.2 and 7.4 [57]). The osteoblast proliferation in indirect contact with the composite exhibited an interesting pattern. The cell metabolic activity was about 30 % of the control on day 1, remained unchanged on day 3, and then increased sharply to 80 % of the control by day 7 (i.e. within the cytocompatibility range according to ISO standard 10993-5). This behaviour

can be explained by the dilution of the soluble degradation products with cell culture medium renewal to a cytocompatible level that allows cell proliferation and the observed lethargy in osteoblast proliferation in direct and indirect contact with CDHA [58]. Since the proliferation pattern significantly differs from that observed with the hydrothermally treated scaffolds, which increases the electrolyte pH slightly more, it is most likely that the cell lethargy induced by CDHA was responsible for the initially low metabolic activity rather than cytotoxicity caused by high osmolality and alkalinisation.

The incorporation of CDHA improved the stress-strain response of the WE43 Mg alloy scaffolds by providing additional load-bearing capacity, reducing loading on the Mg alloy struts, and preventing strut buckling. The interpenetration, constriction, and interlocking of phases increased the compressive strength and damage tolerance by facilitating effective stress transfer via the scaffold, leading to strain delocalization, e.g. Ref. [59]. As a result, the composites exhibited an enhanced compressive strength compared to the as-printed Mg alloy scaffolds, with a high load-bearing capacity even under significant strain (Fig. 6c and d). Furthermore, the scaffolds produced by LB-PBF display a surface roughness in the form of powder adheres (Fig. 1b), enhancing mechanical interlocking with CDHA. Nonetheless, the results showed that the compressive strength of the Mg/CDHA-190 composites was lower than the compressive strength of CDHA-190 control (Fig. 6) and that of the implantable WE43 Mg alloy [9], thus this composite is currently not meeting the ideal mechanical requirements for bone fracture reduction. The following reasons are identified for the observed low strength.

First, the composites developed herein contain a significantly lower Mg fraction (only 25 vol%) than the Mg/hydroxyapatite composites reported in the literature [60], aimed at reducing the total hydrogen evolution volume. Second, the α-TCP formulation used herein generates a CDHA with relatively low compressive strength (Fig. 6d). However, CPCs can achieve a compressive strength of up to 150 MPa [61], suggesting the potential to produce composites with a compression strength close to the yield strength of Mg. Third, the α-TCP conversion into CDHA was lower in the composites than in the control CDHA monoliths (Fig. 5). As the compressive strength of CDHA increases with a higher degree of α-TCP conversion [26], the CDHA in the composite is expected to be weaker than the CDHA in the control monolith. This effect of α-TCP conversion is clearly observed between Mg/CDHA-90 and Mg/CDHA-190 composites (Fig. 6d). Despite the Mg-90 and Mg-190 control scaffolds having a similar compressive strength (Fig. 6d), the low conversion of α-TCP resulted in a Mg/CDHA-90 composite with lower strength. The release of Mg^{2+} ions from the scaffold during the hydrothermal treatment is the most likely reason for the lower α-TCP conversion into CDHA, as Mg prevents the hardening of the cement [62].

From a processing standpoint, finding a balance between α-TCP conversion and Mg passivation during the hydrothermal treatment is crucial to enhance the mechanical properties and corrosion resistance of the composites. Since the Mg degradation at 90 °C did not affect the compressive strength and the stress-strain response of the scaffold, a lower treatment temperature is attractive for the optimal processing of the composites. However, at 37 °C, the α-TCP conversion rate is sluggish, and the hydrogen evolution expels the α-TCP paste out of the scaffold before hardening (Fig. 2e). Therefore, additional research is required to confine the paste during hardening in the 37–90 °C temperature range, and to ascertain the time required for complete α-TCP transformation. Furthermore, the kinetics of the transformation can be enhanced by introducing accelerant additives in the α-TCP paste formulation or by infiltrating a faster-setting cement with a higher compressive strength. The addition of Na_2HPO_4 salt in solution in the liquid phase is a straightforward option that increases the conversion rate through the common ion effect [63] without impeding paste injectability [29]. Another appealing processing approach to improve the strength of the composites is to reduce the L/P ratio of the α-TCP paste. The pastes with a lower L/P ratio produce more compact CDHA monoliths with higher compressive strength [64] but also reduce the injectability [29,64], complicating paste infiltration. Nonetheless, lubrication and increased surface energy of the Mg alloy scaffold can facilitate the infiltration at a L/P ratio lower than 0.50 ml/g. In this regard, it is worth mentioning that cooling the α-TCP/poloxamer paste significantly improved infiltration, since the infiltration of the paste at room temperature requires a higher L/P ratio than 0.50 ml/g due to the thermosensitive nature of poloxamer [31].

α-TCP infiltration offers significant advantages over liquid Mg infiltration into hydroxyapatite preforms. The low-temperature processing of the α-TCP paste is much simpler than dealing with molten Mg. While Mg has a low melting point, its strong affinity for oxygen and propensity for evaporation require a protective atmosphere to prevent oxidation, posing challenges in controlling Mg alloys composition. Expensive equipment is needed to infiltrate liquid Mg, and high-temperature reactions and unregulated solidification offer limited control over the microstructure upon infiltration. Specifically, liquid Mg reacts with hydroxyapatite producing Mg_2Ca intermetallic precipitates at the Mg grain boundaries, which introduce microstructural galvanic couples that decrease the composite degradation resistance to about 4–11 mm/year [23]. The high-temperature reactions are avoided by the α-TCP infiltration at room temperature, and the subsequent hydrothermal treatment produces a thick and adherent $Mg(OH)_2$ - $MgCO_3$ - MgO layer at the Mg/hydroxyapatite interface that protects Mg from further degradation, resulting in Mg/CDHA-190 composites with a relatively high degradation resistance (only 1.9 ± 1.0 mm/year). Furthermore, the proper selection of the hydrothermal treatment should allow independent microstructural control of both the Mg and hydroxyapatite components.

5. Conclusion

This work demonstrates the potential of WE43/CDHA interpenetrating phase composites in reducing the mass of Mg alloy in biodegradable implants to minimise hydrogen evolution during degradation. Hydrothermal treatment transforms α-TCP into CDHA, forming a corrosion layer that enhances degradation resistance and offers the advantage of Mg passivation. The composite degradation rate (1.9 ± 1.0 mm/year) approaches that of extruded WE43 Mg alloy (0.25–2.2 mm/year [43,44]), which is significantly lower than that of the as-printed Mg alloy scaffold (17.8 ± 1.2 mm/year). The slower degradation generates less alkalinisation, thereby increasing the cytocompatibility of the scaffolds and composites. Incorporating CDHA in the scaffolds mitigates the adverse effects of porosity on compressive strength by providing additional load-bearing capacity. Despite constituting a low volume fraction (25 %), the Mg alloy scaffold enhances the composite damage tolerance due to continuity and interpenetration with CDHA. Balancing CDHA formation and Mg passivation during hydrothermal processing is essential to enhance both the mechanical and degradation performance of this new family of biodegradable composites for large temporal osteosynthesis devices. The next step to achieve this goal is improving the hydrothermal processing at physiological temperature to prevent Mg structural deterioration while confining the composite to prevent cement expulsion, potentially resulting in composites with superior compressive strength. Enhancing degradation resistance requires improving the LB-PBF processing of the WE43 alloy and developing post-printing treatments to homogenize the microstructure and reduce surface roughness. Optimizing Mg hydrothermal passivation is also crucial for enhancing the degradation resistance of high porosity scaffolds and WE43/CDHA interpenetrating phase composites.

Funding

This work was supported by the Ministry of Health of the Czech Republic (NW24-10-00195). L.D. acknowledges the Brno University of Technology projects CEITEC VUT/FCH-J-23-8367 and CEITEC VUT-J-

24-8642. A special acknowledgement is to CzechNanoLab Research Infrastructure supported by Ministry of Education, Youth and Sports of the Czech Republic (LM2023051) providing access to some devices used for this study.

Data and materials availability

The data that support the findings of this study are available from the corresponding author upon reasonable request.

Ethics approval and consent to participate

Ethics and consent statements do not apply because the manuscript does not include animal studies and human subjects.

CRediT authorship contribution statement

Lenka Drotárová: Writing – original draft, Validation, Investigation, Formal analysis. **Karel Slámečka:** Writing – review & editing, Investigation, Formal analysis. **Tomáš Balint:** Writing – review & editing, Investigation, Formal analysis. **Michaela Remešová:** Investigation, Formal analysis. **Radovan Hudák:** Resources, Methodology. **Jozef Živčák:** Resources, Methodology. **Marek Schnitzer:** Writing – review & editing, Resources, Methodology. **Ladislav Čelko:** Writing – review & editing, Resources, Methodology. **Edgar B. Montufar:** Writing – review & editing, Supervision, Methodology, Conceptualization.

Declaration of competing interest

The authors declare that they have no known competing financial interests or personal relationships that could have appeared to influence the work reported in this paper.

Acknowledgements

The authors acknowledge Adelia Kashimbetova and Pavel Gejdoš from CEITEC-BUT for the support during microscopic observations, and David Kusmič from University of Defence in Brno for the support with optical emission spectroscopy.

References

[1] H. Waizy, J. Diekmann, A. Weizbauer, J. Reifenrath, I. Bartsch, V. Neubert, R. Schavan, H. Windhagen, *In vivo* study of a biodegradable orthopedic screw (MgYREZr-alloy) in a rabbit model for up to 12 months, J. Biomater. Appl. 28 (5) (2014) 667–675, https://doi.org/10.1177/0885328212472215.

[2] C. Plaass, S. Ettinger, L. Sonnow, S. Koenneker, Y. Noll, A. Weizbauer, J. Reifenrath, L. Claassen, K. Daniilidis, C. Stukenborg-Colsman, H. Windhagen, Early results using a biodegradable magnesium screw for modified chevron osteotomies, J. Orthop. Res. 34 (12) (2016) 2207–2214, https://doi.org/10.1002/jor.23241.

[3] C. Plaass, C. Von Falck, S. Ettinger, L. Sonnow, F. Calderone, Bioabsorbable magnesium versus standard titanium compression screws for fixation of distal metatarsal osteotomies – 3 year results of a randomized clinical trial, J. Orthop. Sci. 23 (2) (2018) 321–327, https://doi.org/10.1016/j.jos.2017.11.005.

[4] X.N. Gu, W.R. Zhou, Y.F. Zheng, Y. Cheng, S.C. Wei, S.P. Zhong, T.F. Xi, L.J. Chen, Corrosion fatigue behaviors of two biomedical Mg alloys - AZ91D and WE43 - in simulated body fluid, Acta Biomater. 6 (12) (2010) 4605–4613, https://doi.org/10.1016/j.actbio.2010.07.026.

[5] M. Socjusz-Podosek, L. Litynska, Effect of yttrium on structure and mechanical properties of Mg alloys, Mater. Chem. Phys. 80 (2003) 472–475, https://doi.org/10.1016/S0254-0584(02)00549-7.

[6] D. Liu, Y. Ding, T. Guo, X. Qin, C. Guo, S. Yu, et al., Influence of fine-grain and solid-solution strengthening on mechanical properties and *in vitro* degradation of WE43 alloy, Biomed. Mater. 9 (2014) 015014, https://doi.org/10.1088/1748-6041/9/1/015014.

[7] A. Davenport, C. Padovani, B. Connolly, N. Stevens, T. Beale, A. Groso, M. Stampanoni, Synchrotron X-ray microtomography study of the role of Y in corrosion of magnesium alloy WE43, Electrochem. Solid State Lett. 10 (2) (2007) C5–C8, 10.10.1149/1.2400727.

[8] N. Li, Y.F. Zheng, Novel magnesium alloys developed for biomedical application: a review, J. Mater. Sci. Technol. 29 (6) (2013) 489–502, https://doi.org/10.1016/j.jmst.2013.02.005.

[9] A. Torroni, C. Xiang, L. Witek, E.D. Rodriguez, P.G. Coelho, N. Gupta, Biocompatibility and degradation properties of WE43 Mg alloys with and without heat treatment: *in vivo* evaluation and comparison in a cranial bone sheep model, J. Cranio-Maxillo-Fac. Surg. 45 (12) (2017) 2075–2083, https://doi.org/10.1016/j.jcms.2017.09.016.

[10] F. Witte, V. Kaese, H. Haferkamp, E. Switzer, A. Meyer-Lindenberg, C.J. Wirth, H. Windhagen, *In vivo* corrosion of four magnesium alloys and the associated bone response, Biomaterials 26 (17) (2005) 3557–3563, https://doi.org/10.1016/j.biomaterials.2004.09.049.

[11] F. Witte, J. Fischer, J. Nellesen, H.-A. Crostack, V. Kaese, A. Pisch, *In vitro* and *in vivo* corrosion measurements of magnesium alloys, Biomaterials 27 (2006) 1013–1018, https://doi.org/10.1016/j.biomaterials.2005.07.037.

[12] J. Kuhlmann, I. Bartsch, E. Willbold, S. Schuchardt, O. Holz, N. Hort, D. Höche, W. R. Heineman, F. Witte, Fast escape of hydrogen from gas cavities around corroding magnesium implants, Acta Biomater. 9 (10) (2013) 8714–8721, https://doi.org/10.1016/j.actbio.2012.10.008.

[13] Y. Sun, H. Helmholz, R. Willumeit-Römer, Peri-implant gas accumulation in response to magnesium-based musculoskeletal biomaterials: reframing current evidence for preclinical research and clinical evaluation, J. Magnesium Alloys 12 (1) (2024) 59–71, https://doi.org/10.1016/j.jma.2024.01.023.

[14] K. Gaalen, C. Quinn, M. Weiler, F. Gremse, et al., Predicting localised corrosion and mechanical performance of a PEO surface modified rare earth magnesium alloy for implant use through *in-silico* modelling, Bioact. Mater. 26 (2023) 437–451, https://doi.org/10.1016/j.bioactmat.2023.03.009.

[15] C. Wang, J. Liu, S. Min, Y. Liu, B. Liu, Y. Hu, Z. Wang, F. Mao, C. Wang, X. Ma, P. Wen, Y. Zheng, Y. Tian, The effect of pore size on the mechanical properties, biodegradation and osteogenic effects of additively manufactured magnesium scaffolds after high temperature oxidation: an *in vitro* and *in vivo* study, Bioact. Mater. 6 (28) (2023) 537–548, https://doi.org/10.1016/j.bioactmat.2023.06.009.

[16] E. Fiume, G. Magnaterra, A. Rahdar, E. Verné, F. Baino, Hydroxyapatite for biomedical applications: a short overview, Ceramics 4 (4) (2021) 542–563, https://doi.org/10.3390/ceramics4040039.

[17] F. Witte, F. Feyerabend, P. Maier, J. Fischer, M. Störmer, C. Blawert, W. Dietzel, N. Hort, Biodegradable magnesium-hydroxyapatite metal matrix composites, Biomaterials 28 (13) (2007) 2163–2174, https://doi.org/10.1016/j.biomaterials.2006.12.027.

[18] A.K. Khanra, H.C. Jung, S.H. Yu, K.S. Hong, K.S. Shin, Microstructure and mechanical properties of Mg-HAP composites, Bull. Mater. Sci. 33 (2010) 43–47, https://doi.org/10.1007/s12034-010-0006-z.

[19] X. Wang, L.H. Dong, J.T. Li, X.L. Li, X.L. Ma, Y.F. Zheng, Microstructure, mechanical property and corrosion behavior of interpenetrating (HA+β-TCP)/MgCa composite fabricated by suction casting, Mater. Sci. Eng., C 33 (7) (2013) 4266–4273, https://doi.org/10.1016/j.msec.2013.06.018.

[20] X.N. Gu, X. Wang, N. Li, L. Li, Y.F. Zheng, X. Miao, Microstructure and characteristics of the metal-ceramic composite (MgCa-HA/TCP) fabricated by liquid metal infiltration, J. Biomed. Mater. Res., Part B 99B (1) (2011) 127–134, https://doi.org/10.1002/jbm.b.31879.

[21] X. Wang, J.T. Li, M.Y. Xie, L.J. Qu, P. Zhang, X.L. Li, Structure, mechanical property and corrosion behaviors of (HA+β-TCP)/Mg-5Sn composite with interpenetrating networks, Mater. Sci. Eng., C 1 (56) (2015) 386–392, https://doi.org/10.1016/j.msec.2015.06.047.

[22] B. Chen, K. Yin, T.-F. Lu, B.-Y. Sun, Q. Dong, C. Lu, Z.-C. Li, AZ91 magnesium alloy/porous hydroxyapatite composite for potential application in bone repair, J. Mater. Sci. Technol. 32 (2016) 858–864, https://doi.org/10.1016/j.jmst.2016.06.010.

[23] M. Casas-Luna, E.B. Montufar, N. Hort, S. Díaz-de-la-torre, J.C. Méndez-García, L. Vištejnová, A. Brinek, A. Danhel, K. Dvořák, J. Kaiser, L. Čelko, Degradable magnesium-hydroxyapatite interpenetrating phase composites processed by current assisted metal infiltration in additive-manufactured porous preforms, J. Magnesium Alloys 10 (12) (2022) 3641–3656, https://doi.org/10.1016/j.jma.2022.07.019.

[24] M. Bohner, Calcium orthophosphates in medicine: from ceramics to calcium phosphate cements, Injury 31 (Suppl 4) (2000) 37–47, https://doi.org/10.1016/s0020-1383(00)80022-4.

[25] C.D. Friedman, P.D. Costantino, S. Takagi, L.C. Chow, BoneSource hydroxyapatite cement: a novel biomaterial for craniofacial skeletal tissue engineering and reconstruction, J. Biomed. Mater. Res. 43 (4) (1998) 428–432, https://doi.org/10.1002/(sici)1097-4636(199824)43:4<428::aid-jbm10>3.0.co;2-0.

[26] M.P. Ginebra, E. Fernández, E.A. De Maeyer, R.M. Verbeeck, M.G. Boltong, J. Ginebra, F.C. Driessens, J.A. Planell, Setting reaction and hardening of an apatitic calcium phosphate cement, J. Dent. Res. 76 (4) (1997) 905–912, https://doi.org/10.1177/00220345970760041201.

[27] C. Durucan, P.W. Brown, alpha-Tricalcium phosphate hydrolysis to hydroxyapatite at and near physiological temperature, J. Mater. Sci. Mater. Med. 11 (6) (2000) 365–371, https://doi.org/10.1023/a:1008934024440.

[28] A. Barba, A. Diez-Escudero, Y. Maazouz, K. Rappe, et al., Osteoinduction by foamed and 3D-printed calcium phosphate scaffolds: effect of nanostructure and pore architecture, ACS Appl. Mater. Interfaces 9 (48) (2017) 41722–41736, https://doi.org/10.1021/acsami.7b14175.

[29] E.B. Montufar, Y. Maazouz, M.P. Ginebra, Relevance of the setting reaction to the injectability of tricalcium phosphate pastes, Acta Biomater. 9 (4) (2013) 6188–6198, https://doi.org/10.1016/j.actbio.2012.11.028.

[30] U. Gbureck, K. Spatz, R. Thull, J.E. Barralet, Rheological enhancement of mechanically activated alpha-tricalcium phosphate cements, J. Biomed. Mater. Res. B Appl. Biomater. 73 (1) (2005) 1–6, https://doi.org/10.1002/jbm.b.30148.

[31] Y. Maazouz, E.B. Montufar, J. Malbert, M. Espanol, M.P. Ginebra, Self-hardening and thermoresponsive alpha tricalcium phosphate/pluronic pastes, Acta Biomater. 49 (2017) 563–574, https://doi.org/10.1016/j.actbio.2016.11.043.
[32] S. Raymond, Y. Maazouz, E.B. Montufar, R.A. Perez, B. González, J. Konka, J. Kaiser, M.P. Ginebra, Accelerated hardening of nanotextured 3D-plotted self-setting calcium phosphate inks, Acta Biomater. 75 (2018) 451–462, https://doi.org/10.1016/j.actbio.2018.05.042.
[33] Y. Shachaf, M. Gonen-Wadmany, D. Seliktar, The biocompatibility of PluronicF127 fibrinogen-based hydrogels, Biomaterials 31 (10) (2010) 2836–2847, https://doi.org/10.1016/j.biomaterials.2009.12.050.
[34] J.J. Escobar-Chávez, M. López-Cervantes, A. Naïk, Y.N. Kalia, D. Quintanar-Guerrero, A. Ganem-Quintanar, Applications of thermo-reversible pluronic F-127 gels in pharmaceutical formulations, J. Pharm. Pharmaceut. Sci. 9 (3) (2006) 339–358.
[35] H.Y. Lei, R. Yue, Z.J. Xu, Q.H. Wang, Parametric design of Voronoi-based lattice porous structures, Mater. Des. 191 (2020) 108607, https://doi.org/10.1016/j.matdes.2020.108607.
[36] A. Kashimbetova, K. Slámečka, M. Casas-Luna, C. Oliver-Urrutia, S. Ravaszová, K. Dvořák, L. Čelko, E.B. Montufar, Implications of unconventional setting conditions on the mechanical strength of synthetic bone grafts produced with self-hardening calcium phosphate pastes, Ceram. Int. 48 (5) (2022) 6225–6235, https://doi.org/10.1016/j.ceramint.2021.11.163.
[37] Z. Shi, M. Liu, A. Atrens, Measurement of the corrosion rate of magnesium alloys using Tafel extrapolation, Corrosion Sci. 9 (2) (2010) 579–588, https://doi.org/10.1016/j.corsci.2009.10.016.
[38] T. Lu, Z. Sun, C. Jia, J. Ren, J. Li, Z. Ma, J. Zhang, J. Li, T. Zhang, Q. Zang, B. Yang, P. Yang, D. Wang, H. Li, J. Qin, X. He, Roles of irregularity of pore morphology in osteogenesis of Voronoi scaffolds: from the perspectives of MSC adhesion and mechano-regulated osteoblast differentiation, J. Biomech. 151 (5) (2023) 6225–6235, https://doi.org/10.1016/j.jbiomech.2023.111542.
[39] H. Liang, Y. Yang, D. Xie, L. Li, N. Mao, C. Wang, Z. Tian, Q. Jiang, L. Shen, Trabecular-like Ti-6Al-4V scaffolds for orthopedic: fabrication by selective laser melting and *in vitro* biocompatibility, J. Mater. Sci. Technol. 35 (7) (2019) 1284–1297, https://doi.org/10.1016/j.jmst.2019.01.012.
[40] X. Yue, J. Shang, M. Zhang, B. Hur, X. Ma, Additive manufacturing of high porosity magnesium scaffolds with lattice structure and random structure: a study on laser powder bed fusion manufacturing for biomedical implants, Mater. Sci. Eng. A 859 (1) (2022) 144167, https://doi.org/10.1016/j.msea.2022.144167.
[41] M. Araya, M. Jaskari, T. Rautio, T. Guillén, A. Järvenpää, Assessing the compressive and tensile properties of TPMS-Gyroid and stochastic Ti64 lattice structures: a study on laser powder bed fusion manufacturing for biomedical implants, J. Sci.: Advanced Materials and Devices 9 (1) (2024) 100663, https://doi.org/10.1016/j.jsamd.2023.100663.
[42] J. Liu, B. Liu, S. Min, B. Yin, B. Peng, Z. Yu, C. Wang, X. Ma, P. Wen, Y. Tian, Y. Zheng, Biodegradable magnesium alloy WE43 porous scaffolds fabricated by laser powder bed fusion for orthopedic applications: process optimization, *in vitro* and *in vivo* investigation, Bioact. Mater. 24 (16) (2022) 301–319, https://doi.org/10.1016/j.bioactmat.2022.02.020.
[43] A.H.M. Sanchez, B.J.C. Luthringer, F. Feyerabend, R. Willumeit, Mg and Mg alloys: how comparable are *in vitro* and *in vivo* corrosion rates? A review, Acta Biomater. 13 (2015) 16–31, https://doi.org/10.1016/j.actbio.2014.11.048.
[44] X. Zhang, G. Yuan, L. Mao, J. Niu, W. Ding, Biocorrosion properties of as-extruded Mg–Nd–Zn–Zr alloy compared with commercial AZ31 and WE43 alloys, Mater. Lett. 66 (1) (2012) 209–211, https://doi.org/10.1016/j.matlet.2011.08.079.
[45] O.E. Sotomayor, H.V. Tippur, Role of cell regularity and relative density on elastoplastic compression response of 3-D open-cell foam core sandwich structure generated using Voronoi diagrams, Acta Mater. 78 (2014) 301–313, https://doi.org/10.1016/j.actamat.2014.06.051.
[46] J. Li, Y. Yang, Z. Sun, K. Peng, K. Liu, P. Xu, J. Li, X. Wei, X. He, Integrated evaluation of biomechanical and biological properties of the biomimetic structural bone scaffold: biomechanics, simulation analysis, and osteogenesis, Materials Today Bio 24 (2024) 100934, https://doi.org/10.1016/j.mtbio.2023.100934.
[47] F. Bär, L. Berger, L. Jauer, G. Kurtuldu, R. Schäublin, J.H. Schleifenbaum, J. F. Löffler, Laser additive manufacturing of biodegradable magnesium alloy WE43: a detailed microstructure analysis, Acta Biomater. 98 (2019) 36–49, https://doi.org/10.1016/j.actbio.2019.05.056.
[48] H. Hyer, L. Zhou, G. Benson, B. McWilliams, K. Cho, Y. Sohn, Additive manufacturing of dense WE43 Mg alloy by laser powder bed fusion, Addit. Manuf. 33 (2020) 101123, https://doi.org/10.1016/j.addma.2020.101123.
[49] J. Suchy, M. Horynová, L. Klakurková, D. Palousek, D. Koutny, L. Čelko, Effect of laser parameters on processing of biodegradable magnesium alloy WE43 via selective laser melting method, Materials 13 (11) (2020) 2623, https://doi.org/10.3390/ma13112623.
[50] M. Esmaily, Z. Zeng, A.N. Mortazavi, A. Gullino, S. Choudhary, T. Derra, F. Benn, F. D'Elia, M. Müther, S. Thomas, A. Huang, A. Allanore, A. Kopp, N. Birbilis, A detailed microstructural and corrosion analysis of magnesium alloy WE43 manufactured by selective laser melting, Addit. Manuf. 35 (2020) 101321, https://doi.org/10.1016/j.addma.2020.101321.
[51] Y. Zhu, Q. Zhao, Y.-H. Zhang, G. Wu, Hydrothermal synthesis of protective coating on magnesium alloy using de-ionized water, Surf. Coating. Technol. 206 (11–12) (2012) 2961–2966, https://doi.org/10.1016/j.surfcoat.2011.12.029.
[52] F. Iqbal, A. Ali, M. Naveed, F. Ikram, H. Fatima, Hydrothermal deposition of high strength biocompatible magnesium phosphate coating through *in situ* conversion of AZ91D-3Ca magnesium substrate, Surf. Coating. Technol. 457 (2023) 129301, https://doi.org/10.1016/j.surfcoat.2023.129301.
[53] Y. Yang, C. He, D. E, W. Yang, F. Qi, D. Xie, L. Shen, S. Peng, C. Shuai, Mg bone implant: features, developments and perspectives, Mater. Des. 185 (2019) 108259, https://doi.org/10.1016/j.matdes.2019.108259.
[54] K. Munir, A. Biesiekierski, C. Wen, Y. Li, Biodegradable Alloys. Structural Biomaterials, 2021, pp. 189–228, https://doi.org/10.1016/B978-0-12-818831-6.00001-X.
[55] F. Benn, N. Kröger, M. Zinser, K. van Gaalen, T.J. Vaughan, M. Yan, R. Smeets, E. Bibiza, S. Malinov, F. Buchanan, A. Kopp, Influence of surface condition on the degradation behaviour and biocompatibility of additively manufactured WE43, Mater. Sci. Eng. C 124 (2021) 112016, https://doi.org/10.1016/j.msec.2021.112016.
[56] S.S. Ozturk, B.O. Palsson, Effect of medium osmolarity on hybridoma growth, metabolism, and antibody production, Biotechnol. Bioeng. 37 (10) (1991) 989–993, https://doi.org/10.1002/bit.260371015.
[57] R.I. Freshney, Culture of Animal Cells, John Wiley & Sons, Inc., 2010, https://doi.org/10.1002/9780470649367.
[58] J.M. Sadowska, J. Guillem-Marti, E.B. Montufar, M. Espanol, M.P. Ginebra, Biomimetic versus sintered calcium phosphates: the *in vitro* behavior of osteoblasts and mesenchymal stem cells, Tissue Eng. 23 (23–24) (2017) 1297–1309, https://doi.org/10.1089/ten.TEA.2016.0406.
[59] Y. Liu, B. Chen, Z. Liu, Z. Zhang, R.O. Ritchie, Bioinspired interpenetrating-phase metal composites, Prog. Mater. Sci. 144 (2024) 101281, https://doi.org/10.1016/j.pmatsci.2024.101281.
[60] F. Khorashadizade, S. Abazari, M. Rajabi, H. Bakhsheshi-Rad, A. Ismail, S. Sharif, S. Ramakrishna, F. Berto, Overview of magnesium-ceramic composites: mechanical, corrosion and biological properties, J. Mater. Res. Technol. 15 (2021) 6034–6066, https://doi.org/10.1016/j.jmrt.2021.10.141.
[61] U. Gbureck, J.E. Barralet, K. Spatz, L.M. Grover, R. Thull, Ionic modification of calcium phosphate cement viscosity. Part I: hypodermic injection and strength improvement of apatite cement, Biomaterials 25 (11) (2004) 2187–2195, https://doi.org/10.1016/j.biomaterials.2003.08.066.
[62] M.P. Ginebra, M.G. Boltong, E. Fernández, et al., Effect of various additives and temperature on some properties of an apatitic calcium phosphate cement, J. Mater. Sci. Mater. Med. 6 (1995) 612–616, https://doi.org/10.1007/BF00121286.
[63] E. Fernández, M.G. Boltong, M.P. Ginebra, O. Bermúdez, F.C.M. Driessens, J. A. Planell, Common ion effect on some calcium phosphate cements, Clin. Mater. 16 (2) (1994) 99–103, https://doi.org/10.1016/0267-6605(94)90103-1.
[64] R.M. O'Hara, N.J. Dunne, J.F. Orr, et al., Optimisation of the mechanical and handling properties of an injectable calcium phosphate cement, J. Mater. Sci. Mater. Med. 21 (2010) 2299–2305, https://doi.org/10.1007/s10856-009-3977-9.